minerals

MDPI

Article

Garnet Geochemistry of Reduced Skarn System: Implications for Fluid Evolution and Skarn Formation of the Zhuxiling W (Mo) Deposit, China

Xiao-Xia Duan [1,2,*], Ying-Fu Ju [1,2], Bin Chen [3] and Zhi-Qiang Wang [1,2]

1 School of Resources and Environmental Engineering, Hefei University of Technology, Hefei 230009, China; 2019110708@mail.hfut.edu.cn (Y.-F.J.); wangzq@hfut.edu.cn (Z.-Q.W.)
2 Ore Deposit and Exploration Center (ODEC), Hefei University of Technology, Hefei 230009, China
3 Department of Earth and Space Sciences, Southern University of Science and Technology, Shenzhen 518055, China; chenb6@sustech.edu.cn
* Correspondence: duanxiaoxia@hfut.edu.cn

Received: 21 October 2020; Accepted: 12 November 2020; Published: 17 November 2020

Abstract: A newly discovered tungsten ore district containing more than 300,000 tons of WO_3 in southern Anhui Province has attracted great attention. The Zhuxiling W (Mo) deposit in the district is dominated by skarn tungsten mineralization. This paper conducted in suit EPMA and LA-ICPMS spot and mapping analysis of the skarn mineral garnet to reveal the evolution of fluids, metasomatic dynamics, and formation conditions of skarn. Two generations of garnet have been identified for Zhuxiling W (Mo) skarn: 1) Gt-I generation garnet is isotropic, Al-rich grossular without zoning. As a further subdivision, Gt-IB garnet ($Adr_{19-46}Grs_{49-77}$ $(Sps+Pyr+Alm)_{4-5}$) contains significantly high content of Ti and Mn compared with Gt-IA garnet ($Adr_{3-42}Grs_{53-96}$ $(Sps+Pyr+Alm)_{1-5}$). 2) Gt-II generation garnet is anisotropic, Fe-rich andradite with oscillatory zoning. Gt-II garnet displays compositional changes with a decrease of Fe and an increase of Mn from proximal skarn (Gt-IIA) to distal skarn (Gt-IIB) with the presence of subcalcic garnet for Gt-IIB type (Sps+Pyr+Alm = 56–68). The presence of pyrrhotite associated with subcalcic garnet indicates a relatively reduced skarn system. Gt-I grossular is overall enriched in Cr, Zr, Y, Nb, and Ta compared with the Gt-II andradite, and both W and Sn strongly favor Fe-rich garnet compared with Al-rich garnet. Gt-IA grossular garnet presents a REE trend with an upward-facing parabola peaking at Pr and Nd in contrast to low and flat HREE, and Gt-IB grossular garnet has a distinct REE pattern with enriched HREE. Gt-IIA andradite garnet displays a right-dipping REE pattern (enriched LREE and depleted HREE) with a prominent positive Eu anomaly (Eu/Eu* = 3.6–15.3). In contrast, Gt-IIB andradite garnet shows depleted LREE and enriched HREE with a weak positive Eu anomaly (Eu/Eu* = 0–6.0). The incorporation and fractionation of REE in garnet are collectively controlled by crystal chemistry and extrinsic factors, such as P–T–X conditions of fluids, fluid/rock ratios, and mineral growth kinetics. Major and trace elements of two generations of garnet combined with optical and textural characteristics suggest that Gt-I Al-rich grossular garnets grow slowly through diffusive metasomatism under a closed system, whereas Gt-II Fe-rich andradite represent rapid growth garnet formed by the infiltration metasomatism of magmatic fluids in an open system. The Mn-rich garnet implies active fluid–rock interaction with Mn-rich dolomitic limestone of the Lantian Group in the district.

Keywords: LA-ICPMS; Jiangnan tungsten ore belt; Zhuxiling W (Mo) deposit; reduced skarn; Mn-rich garnet

1. Introduction

Mineralogy is fundamental in the definition and study of skarn and skarn deposits [1], as it can provide insight into skarn formations and evaluate their potential for economic importance. As an indicator mineral, garnet composition and texture can effectively reveal the physical and chemical properties of ore-forming fluids and record hydrothermal fluid evolution and water–rock reactions [1–4]. Moreover, garnet chemistry is widely used to reveal skarn formation processes such as the metasomatism mechanism (diffusive metasomatism or advective metasomatism, [3,5]) and the kinetics of mineral growth [6]. Garnets from different skarn deposits (i.e., W, Sn, Cu, and Mo) show enrichment of respective metal elements and demonstrate potential as an indicator for mineralization exploration [7–10].

Recent exploration revealed a NE trending tungsten ore belt, namely the Jiangnan porphyry−skarn tungsten ore belt [11], with many large tungsten deposits located within the Jiangnan orogenic belt, including the giant Zhuxi and Dahutang tungsten deposits in northern Jiangxi Province and numerous W (Mo) deposits in southern Anhui Province. However, few studies have focused on the ore district in Anhui Province [12–15], leading to a lack of detailed mineralogical and geochemical work on skarn minerals. This paper reports new major and trace element data of different types of garnet occurrences in the Zhuxiling deposit, a typical skarn W (Mo) deposit in southern Anhui Province. Based on compositional variation and optical and textural characteristics, we discuss the mechanism and controlling factors for incorporation of trace element (REE in particular) into garnet and constrain the evolution of metasomatic fluids and physicochemical conditions during skarn mineralization from spatial and temporal perspectives.

2. Regional Geological Settings and Ore Deposit Geology

The Jiangnan orogenic belt (JNB) is a Neoproterozoic subduction-collisional zone between the Yangtze and the Cathaysia blocks [16–18]. The JNB is composed of a Precambrian basement and a Phanerozoic sequence. The basement consists mainly of Neoproterozoic volcanoclastic and sedimentary rocks. The overlying Phanerozoic sequence includes the Silurian to Early Jurassic marine clastic and carbonate rocks, Middle Jurassic sedimentary and volcanic rocks, and Cretaceous red-bed sandstone. There are mainly two periods of magmatic events, represented by Jinningian and Yanshanian granitic rocks. The Jinningian intrusions (~821 Ma) are mainly biotite granodiorite and fine-grained granite, including the Jiuling, Xucun, Shexian, and Xiuning plutons. The Yanshanian intrusions in the JNB are further divided as the 149−136 Ma W-related granitoids and the 129−102 Ma W- or Sn-related monzonitic granite [19].

Recent exploration revealed many large-scale tungsten deposits in the Jiangnan orogenic belt (Figure 1), including the giant Zhuxi and Dahutang tungsten deposits in northern Jiangxi Province and numerous W (Mo) deposits in southern Anhui Province. All together those tungsten deposits constitute a NE trending tungsten ore belt, namely the Jiangnan porphyry−skarn tungsten ore belt [11], adjacent to the Middle-Lower Yangtze metallogenic belt (Figure 1). The tungsten ore district in southern Anhui Province hosts more than 50 W(Mo) deposits or occurrences and contains more than 300,000 tons of WO_3 [20,21] which include the Dongyuan W (Mo), Zhuxiling W (Mo), Baizhangyan W (Mo), Xiaoyao W−Mo, and Gaojiabang W−Mo deposits [12–15]. The ore-formation ages are confined within 152−143 Ma and are associated with the Jurassic magmatic activity between 152–139 Ma [22].

The Zhuxiling deposit is a large-scale skarn-type tungsten deposit, situated in Ningguo, a city located in southern Anhui province (Figure 2). The exposed strata in the district are the Neoproterozoic Nantuo and Lantian groups, which consist of tuffaceous gravel-bearing sandstone and pelitic dolomitic limestone, respectively. The dolomitic limestone of the Liantian Group is locally Mn-rich [24]. Magmatic rocks in the district are mainly the Late Mesozoic granodiorite, granodiorite porphyry, and granite porphyry veins. The ore-related granodiorite porphyry has an outcrop area of 1.5 km^2, with zircon U−Pb ages of 139−142 Ma [24,25]. The Zhuxiling W(Mo) deposit, which also contains appreciable Ag, comprises mainly two types of mineralization, the skarn/porphyritic W-Mo mineralization and quartz vein type Ag mineralization. The skarn type W-Mo mineralization occurs within the granodiorite

porphyry body as well as along the contact between the granodiorite porphyry and the dolomitic limestone of the Lantian Group. Ore minerals include scheelite, molybdenite, pyrite, sphalerite, pyrrhotite, chalcopyrite, galena, tetrahedrite, argentite, and silver. Gangue minerals mainly include garnet, diopside, quartz, sericite, and calcite. The associated alterations are predominantly skarn, with subordinate silicificated and hornfelsic alterations. For tungsten mineralization, scheelite is the major ore mineral and occurs predominantly as disseminated and in veins intergrown with retrograde minerals. Associated sulfides include large amounts of pyrrhotite, minor sphalerite, chalcopyrite, and pyrite and traces of magnetite (Figure 3a). Limited studies, such as geochronological, petrological, and geochemical analyses of magmatic rocks and ore-forming fluid, have been conducted [24–27].

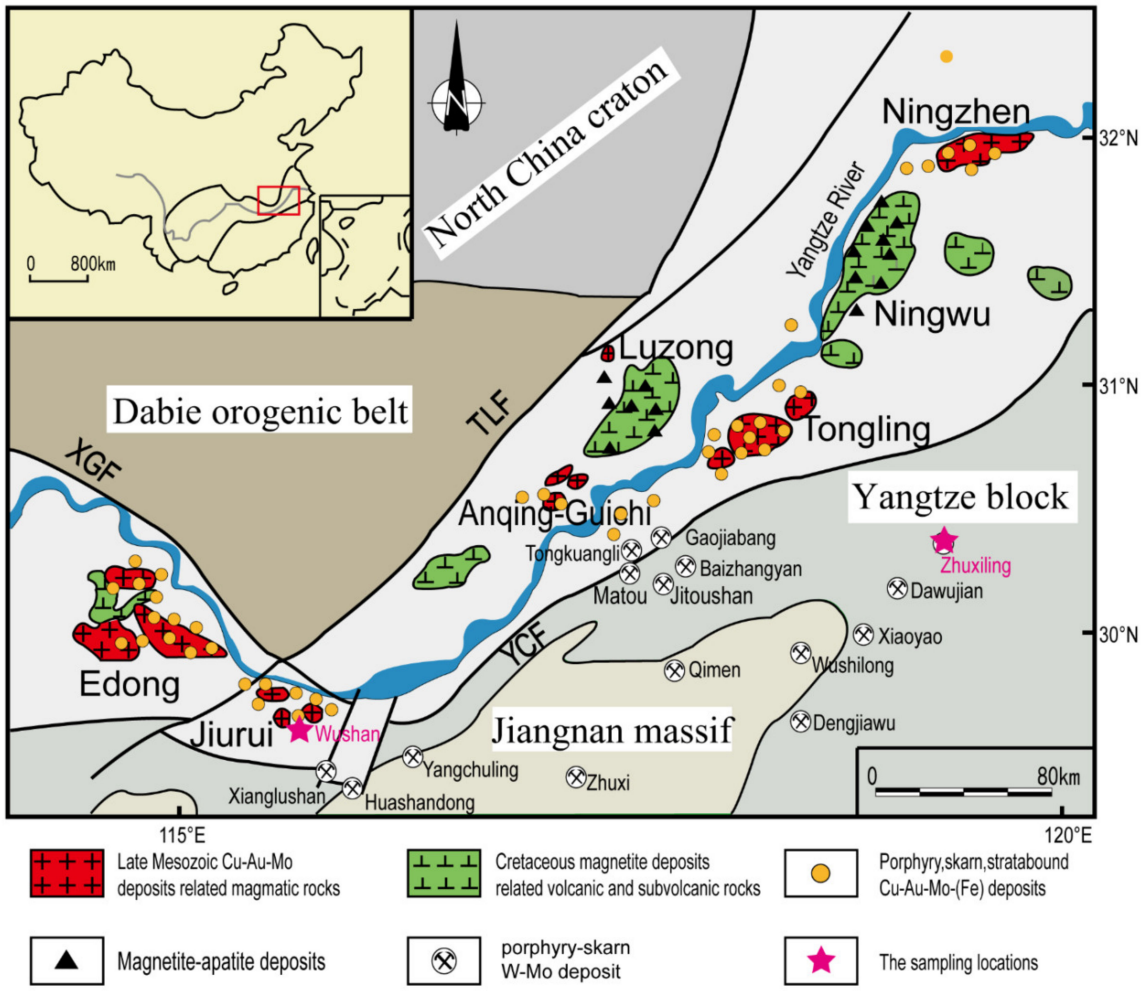

Figure 1. Geological sketch map for the Jiangnan tungsten ore belt showing the location of the Zhuxiling W (Mo) deposit (after [11,23]).

The garnet samples analysed in this study are selected from drill hole ZK502 of the Zhuxiling deposit (Figure 3b–d). Sample ZXL209 is composed predominantly of garnet, quartz, calcite, and diopside, with small amounts of chlorite, titanite, and sphalerite. Sample ZXL211 is diopside-garnet skarn, which is composed mainly of diopside and garnet, as well as minor amounts of sphalerite, pyrite, and scheelite. Mineral assemblages for sample ZXL216 include garnet, diopside, epidote, chlorite, magnetite, pyrite, calcite, and scheelite. The early-stage skarn mineral diopside and garnet are intensively replaced by chlorite, epidote, magnetite, and calcite. Sample ZXL221 is banded skarn, containing mainly garnet and minor amount of chlorite, calcite, and pyrite. Additionally, garnet is widely replaced by calcite and chlorite.

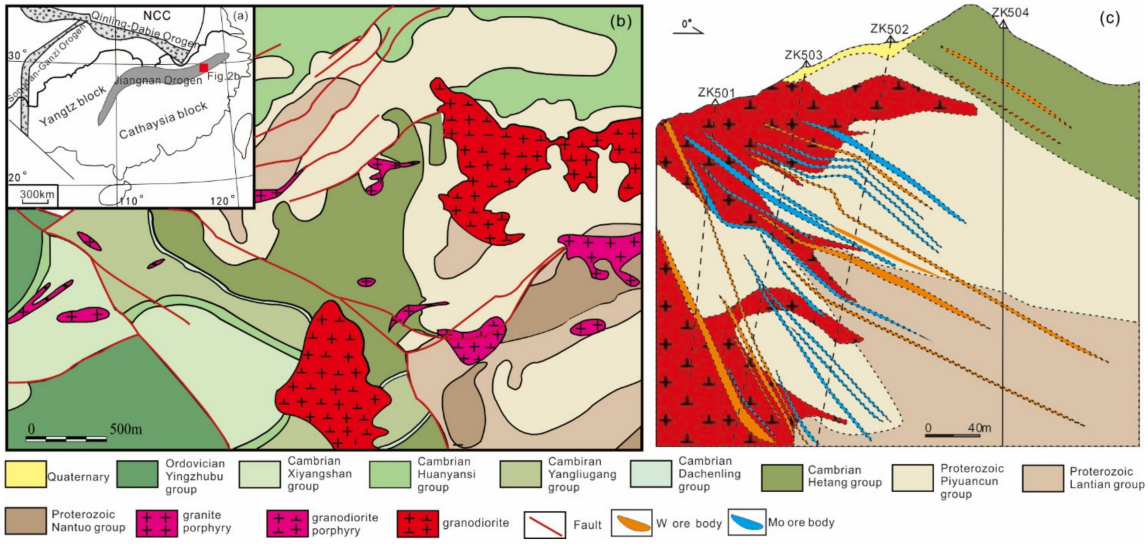

Figure 2. (**a**) Tectonic location of the Jiangnan orogeny; (**b**) geological map of Zhuxiling W(Mo) deposit; (**c**) geological cross section map of the Zhuxiling W (Mo) deposit, illustrating sampling drill hole (after [24]).

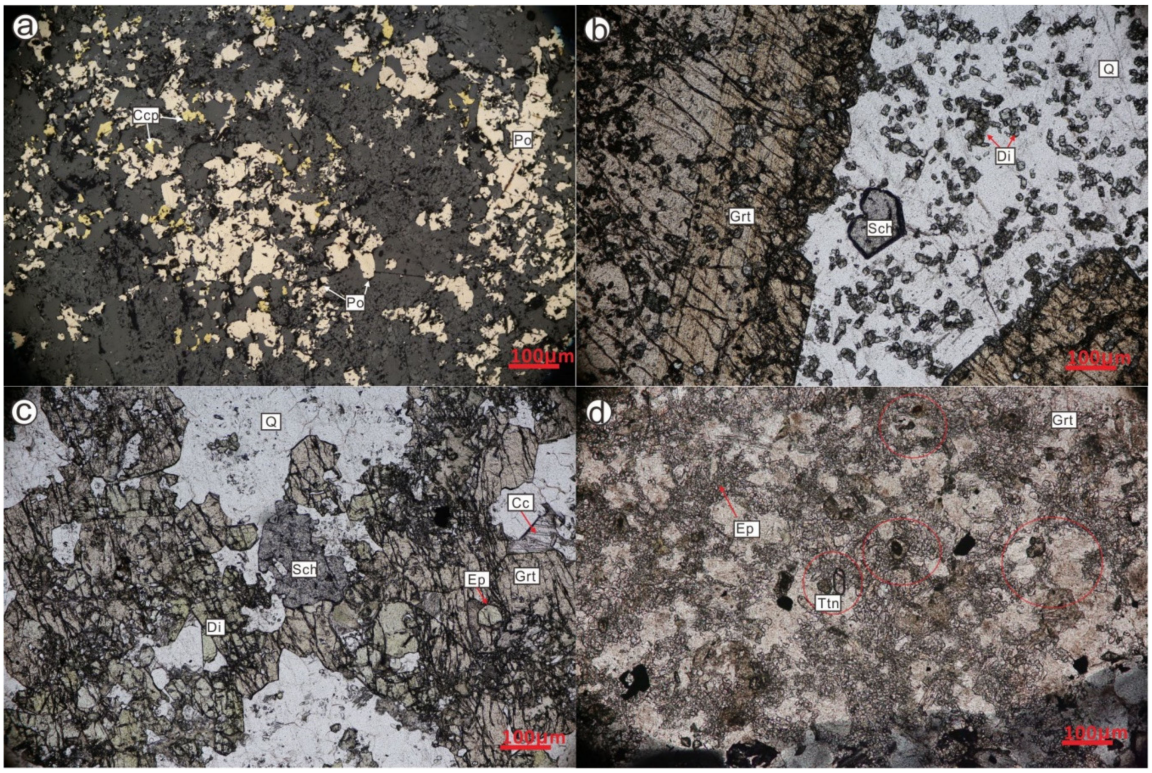

Figure 3. Photomicrographs of skarns from the Zhuxiling W (Mo) deposit. (**a**) Diopside skarn consists of diopside, quartz, and large amounts of pyrrhotite, as well as minor amounts of chalcopyrite and titanite; (**b**) garnet skarn consists of large euhedral garnet crystal, small diopside as inclusions inside quartz and garnet, as well as disseminated scheelite. (**c**) Garnet-diopside skarn where garnet is replaced by epidote, calcite, and scheelite. (**d**) Retrograde skarn with massive epidote, quartz, and disseminated titanite. Abbreviations: Ccp: chalcopyrite; Po: pyrrhotite; Grt: garnet; Sch: scheelite; Di: diopside; Q: quartz; Ep: epidote; Cc: calcite; and Ttn: titanite.

3. Analytical Methods

The major elements of garnet were determined by electron microprobe at the School of Resources and Environmental Engineering at the Hefei University of Technology (HFUT). Backscattered electron (BSE) images were acquired using a JEOL JXA−8900R electron microprobe, and quantitative point analysis of the garnets was conducted using a wavelength-dispersive (WDS) method that employed TAP, PET, and LIF crystals with a 2-μm spatial resolution. Each 120-second analysis was conducted on 2–5 grains for each sample, and the measurement was conducted using an excitation voltage of 15 kV, a beam current of 10 nA, and a spot diameter of 5 μm. The respective peak and background count times were 120 s and 60 s for La, Ce, Sr, and Ba and 60 s and 30 s for all other elements. Garnet molecular formulae were calculated on the basis of 12 oxygen atoms and garnet end-members normative calculations presented proportions of garnet end-members (i.e., grossular (Grs), andradite (Adr), Spessartine (Sps), pyrope (Pyr), and almandine (Alm)) for each analysis.

An in-situ trace element spot and mapping analysis of garnet was performed at HFUT using the Agilent 7900 (quadrupole) ICP−MS coupled with a laser ablation system (PhotonMachines Analyte HE with a 193-nm ArF Excimer). The trace element contents of garnet were measured directly on thin sections. The diameter of the laser beam was 30 μm (with a 10 Hz repetition rate, an output energy of 0.01−0.1 mJ per pulse, and a fluence of ~4 J cm^{-2}). Each analysis consisted of an approximate 30 s background acquisition and 60 s sample acquisition. The dwell time was 3 ms for all REEs and 5 ms for all other elements. Standard reference materials GSE-1g, GSC-1g, BCR-2G, and NIST 612 were used as external standards. The standard reference materials were run after each 10−15 unknowns. Data reduction was performed using ICP−MS DataCal software.

4. Results

Two generations of garnets are identified within the Zhuxiling deposit according to the textural and optical characteristics, which are further divided into four types based on compositional variations. Gt-I generation garnet represents early prograde unzoned garnet, is dark in BSE images, and is replaced by later oscillatory zoned Gt-II generation garnet, which is brighter in BSE images. More specifically, Gt-IA type garnet is colorless under plane polarized light and shows isotropic features with an absence of zoning. Gt-IA garnet is commonly anhedral to subhedral and occurs as irregular-shaped cores encircled by later beige Gt-II oscillatory rims (Figure 4a,b,h). Gt-IA garnet is pervasively modified by retrograde chlorite, scheelite, and calcite. Gt-IB type garnet is also colorless, but it's anisotropic and euhedral compared with Gt-IA garnet. The spotted garnet displays sharp contacts to the later overgrowth of beige garnet. There is no obvious zoning, but it has many cracks filled by massive calcite and quartz inclusions (Figure 4c,e). Gt-IB garnet is relatively scarce and is only observed within the banded skarn (sample ZXL221). Gt-II garnet is subdivided into Gt-IIA and Gt-IIB, representing proximal and distal exoskarn samples, respectively. Gt-II garnet is overall beige under plane polarized light in the form of large euhedral and subhedral crystals. Both the Gt-IIA and Gt-IIB garnet are anisotropic and often exhibit dodecahedral twinning and characteristic oscillatory zoning (Figure 4b,h). In addition to oscillatory zoning, notable irregular zoning was also present for some Gt-IIA garnet shown by BSE imaging (Figure 4f). The trapezohedron {211} faces developing on pre-existing dodecahedral {110} garnets have been observed (Figure 4d). Gt-II garnet contains fine diopside inclusions and is replaced by retrograde minerals such as chlorite, epidote, titanite, tremolite, and calcite.

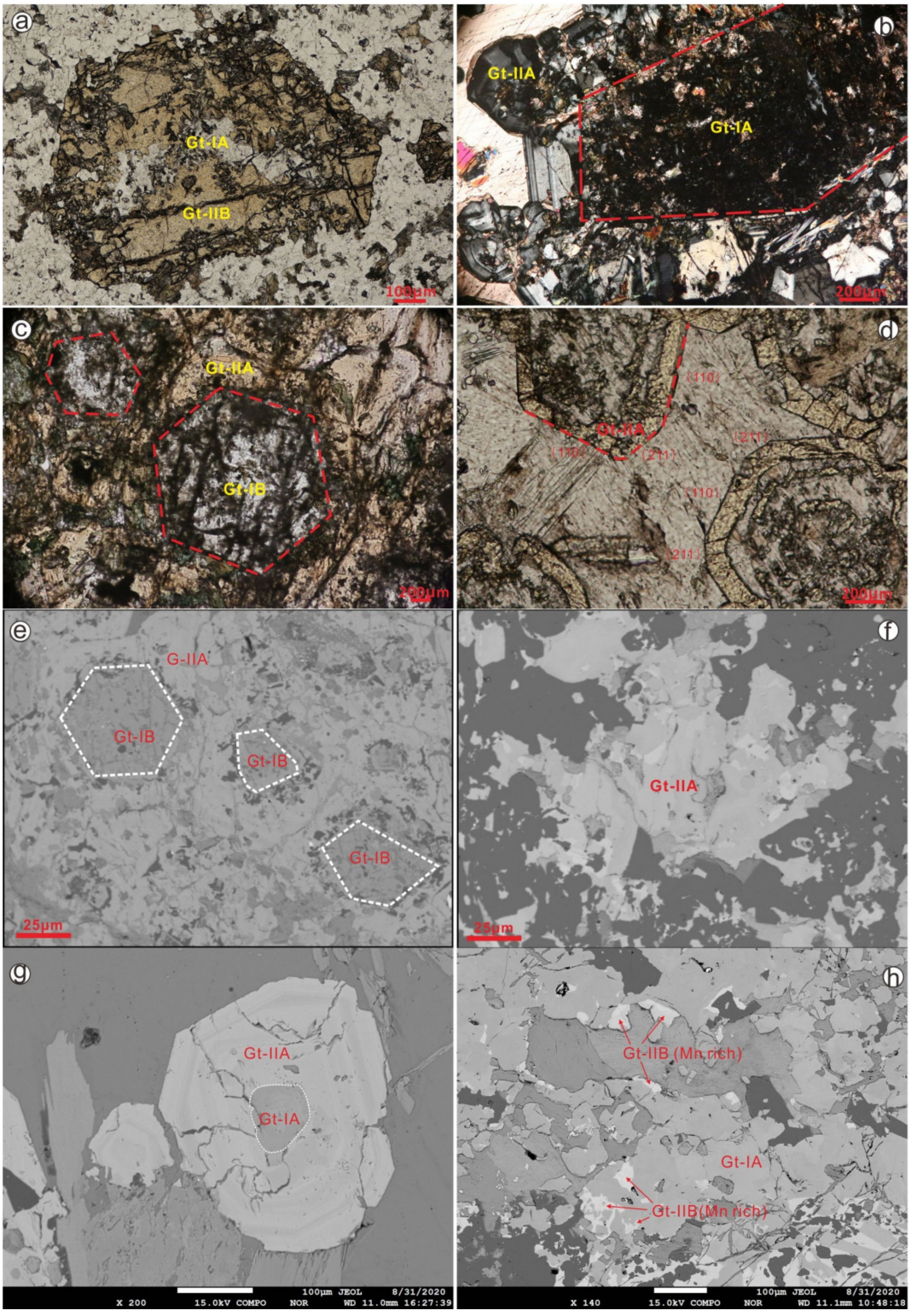

Figure 4. Microscopic and BSE (back scattered electron) characteristics of four types of garnet from the Zhuxiling W (Mo) deposit. (**a**) Pale white Gt-IA garnet is irregularly replaced by beige Gt-IIB garnet; (**b**) Gt-IA is isotropic and shows complete extinction, whereas Gt-IIA garnet is anisotropic with oscillatory zoning; (**c**) spotted euhedral Gt-IB garnet crystal encircled by beige Gt-IIA garnet; (**d**) development of trapezohedron {211} faces in Gt-IIA garnets on pre-existing dodecahedral {110} garnets; (**e**) BSE imaging of euhedral Gt-IB garnet, which is darker than surrounding Gt-IIA garnets; (**f**) patched BSE imaging for typical Gt-IIA garnet; (**g**) BSE image illustrating one euhedral garnet crystal with dark and irregular Gt-IA garnet in the core and oscillatory zoned Gt-IIA garnet in the rim. (**h**) Presence of Mn-rich (spessartine dominate) garnet at the margin of the Gt-IA garnet.

4.1. Major Element Chemistry

The EPMA results for four types of garnets are listed in supplementary Table S1. Garnets have the general chemical formula $X_3Y_2Z_3O_{12}$ (eight formula units per basic cell) and site X corresponds to eight-fold coordination filled by bivalent metal (X = Ca^{2+}, Fe^{2+}, Mg^{2+}, or Mn^{2+}); Y corresponds to six-fold coordination filled by trivalent metal (Y = Al^{3+}, Cr^{3+}, or Fe^{3+}); and Z corresponds to four-fold (tetrahedral) coordination (largely Si). Garnets from the Zhuxiling deposit belong to a grandite solid solution. They have compositions that range from almost pure grossular (Adr_3Grs_{96}) to andradite ($Adr_{85}Grs_{11}$) with variable amounts of spessartine and almandine and traces of pyrope. Different types of garnet show distinct major element compositions (Figure 5), corresponding to the different textural and optical characteristics described before. Gt-IA garnet is characterized by high Al and Mg content and low Fe and Mn content and belongs to grossular ($Adr_{3\text{-}42}Grs_{53\text{-}96}$ $(Sps+Pyr+Alm)_{1\text{-}5}$). Gt-IB garnet is also enriched in Al and depleted in Fe ($Adr_{19\text{-}46}Grs_{49\text{-}77}$ $(Sps+Pyr+Alm)_{4\text{-}5}$) with a significantly high content of Ti (0.08–0.11 apfu) and Mn (0.13–0.15 apfu) compared with Gt-IA garnet (0–0.19 apfu Ti and 0.01–0.05 apfu Mn). Gt-II garnet contains more Fe compared with Gt-I type and is ascribed to andradite. Moreover, the proximal exoskarn Gt-IIA type is Fe-rich andradite ($Adr_{37\text{-}85}Grs_{4\text{-}58}$ $(Sps+Pyr+Alm)_{4\text{-}19}$), whereas the distal exoskarn Gt-IIB is Al-rich andradite ($Adr_{8\text{-}60}Grs_{18\text{-}47}$ $(Sps+Pyr+Alm)_{11\text{-}68}$). Gt-IIB garnet contains elevated Mn (0.28–1.60 apfu) content compared with Gt-IIB garnet (0.09-0.48 apfu). Note that some of Gt-IIB garnet in sample ZXL209 are extremely enriched in Mn (15.834–23.163 wt.%) and those Mn-rich garnet ($Adr_{9\text{-}15}Grs_{18\text{-}35}$ $(Sps+Pyr+Alm)_{56\text{–}68}$) occur as small patches along the margin of Gt-IA grossular (Figure 4g).

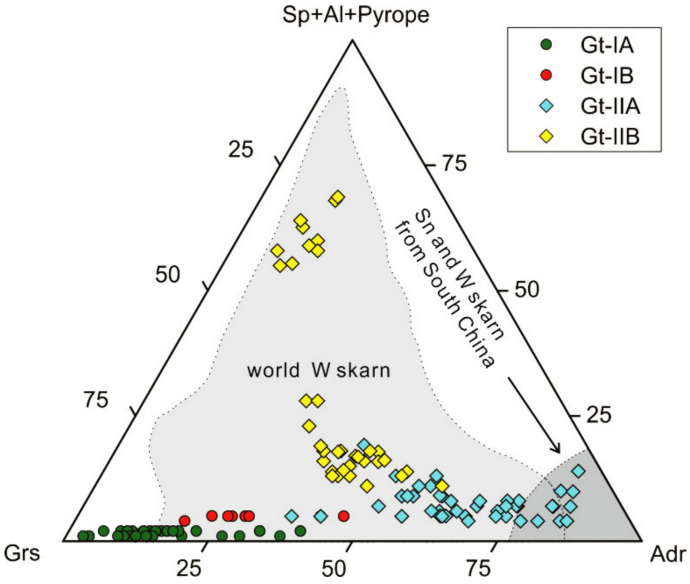

Figure 5. Ternary plots of the garnet compositions from the Zhuxiling W (Mo) deposit. The ranges of garnets in W/Sn skarn around the world are from [1] and the data for Sn and W skarn in South China are from [28].

4.2. Trace Element Chemistry

The trace element data of garnets analyzed by LA-ICPMS are presented in supplementary Table S2. Since the Mn-rich garnet is very small, only two valid spots were obtained. There is no difference between the different types of garnet regarding the large ion lithophile elements (LILE) since all garnets show negligible amounts of LILEs, such as Rb, Cs, Sr, and Ba (Table S2). In contrast, Cr, V, Ga, Zn, Sn, and high field-strength elements (HFSE), such as Zr, Hf, Y, and Sc, are more abundant and show variations corresponding to major element and petrographic features. Gt-I generation grossular is enriched in Cr, Zr, Y, Nb, and Ta and depleted in V, W, and Sn compared with Gt-II

generation andradite (Figure 6). Most trace elements (e.g., Zr, Y, W, and Cr) of Gt-II andradite are more scattered compared with those of Gt-I grossular. More specifically, most of the trace element contents in Gt-IA are comparable to those of Gt-IB, with the exception of Cr. The Gt-IB garnet hosts an extremely high content of Cr (1516–9426 ppm, average of 3639 ppm), whereas the Cr content of Gt-IA garnet is almost 2 orders of magnitude lower (4.6–157 ppm, average of 37 ppm). Gt-II generation andradite has significantly higher V, W, and Sn content compared with Gt-I grossular, and Gt-IIB type andradite contains elevated Zr, Y, Nb, Ta, and Ge in contrast to Gt-IIA type andradite, which shows higher U content (Figure 6). The new trace element analysis of the Zhuxiling W (Mo) deposit confirms that the Fe-rich end-members of grandite are more Sn-enriched, consistent with previous studies [8,9,29].

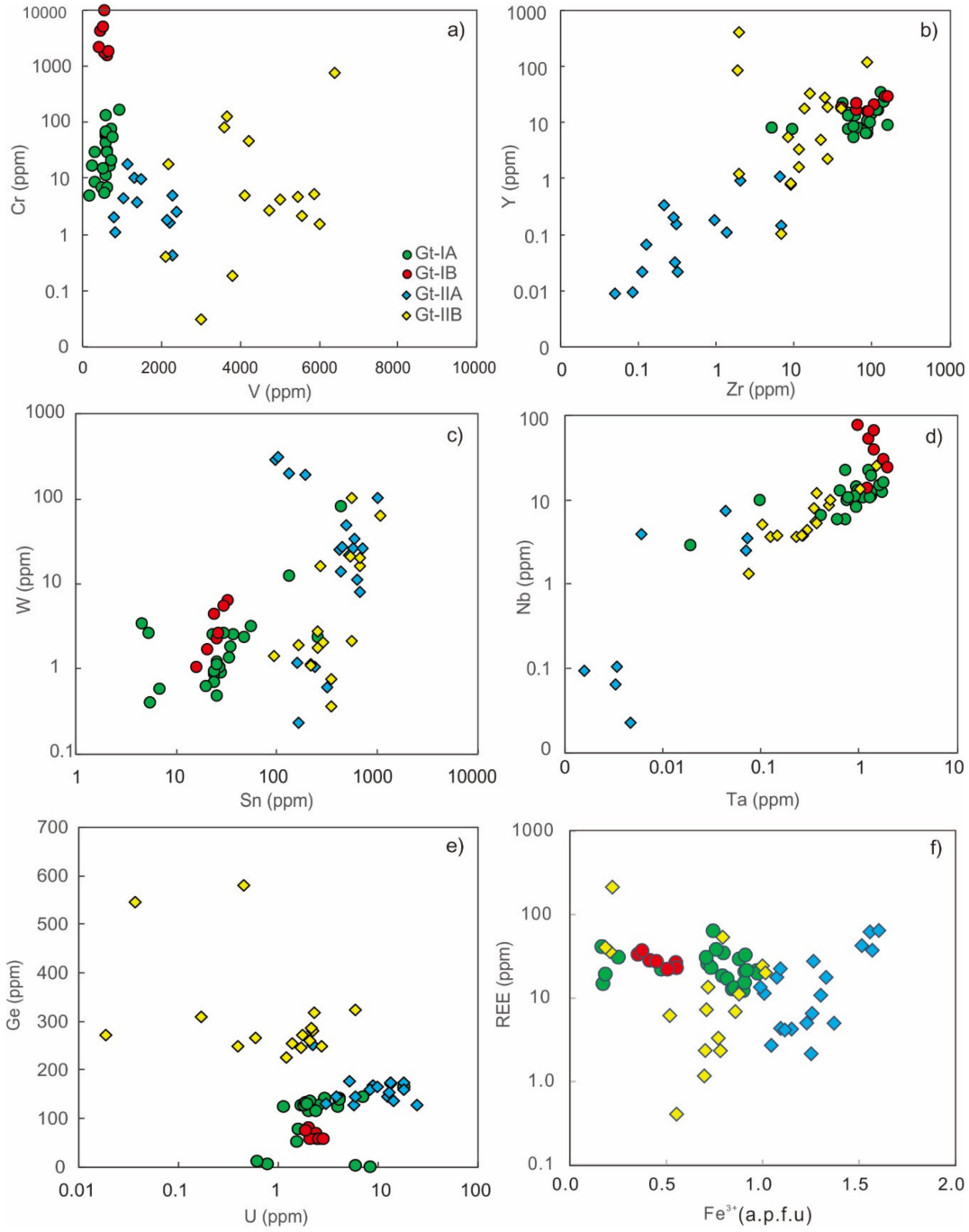

Figure 6. Trace element diagrams of different types of garnets from the Zhuxiling W (Mo) deposit. (**a**) Cr (ppm) versus V(ppm) plot; (**b**) Zr (ppm) versus Y (ppm) plot; (**c**) Sn (ppm) versus W (ppm) plot;

(**d**) Ta (ppm) versus Nb (ppm) plot; (**e**) U (ppm) versus Ge (ppm) plot; (**f**) Fe^{3+} (a.p.f.u) versus REE (ppm) plot.

Despite having the similar average REE content, the REE contents for Gt-II andradite is more dispersed (0.4–214 ppm), whereas the Gt-I grossular are constrained within a narrow range (12.3–64.3 ppm). Moreover, the chondrite-normalized REE pattern of Gt-IA grossular garnet presents a trend with an upward-facing parabola peaking at Pr and Nd, in contrast to low and flat HREE (Figure 7a), due to the closer ionic radii of Pr^{3+} and Nd^{3+} to Ca^{2+}, which is favorable for substitution [30]. Gt-IB grossular has a distinct REE pattern with enriched HREE and depleted LREE (Figure 7b). Both the Gt-IA and Gt-IB grossulars exhibit identical weak negative Eu anomalies (Eu/Eu* = 0.3–1.5 and 0.4–0.9, respectively). On the other hand, Gt-IIA andradite displays a right-dipping REE pattern (enriched LREE and depleted HREE) with a prominent positive Eu anomaly (Eu/Eu* = 3.6–15.3) (Figure 7c). The HREE contents of Gt-IIA andradite are very low with many analyses below detection limits. In comparison, Gt-IIB andradite shows an upward-slopping REE trend manifested by depleted LREE and enriched HREE with weak to no positive Eu anomalies (Eu/Eu* = 0–6.0). Limited analyses of Mn-rich garnets (Sps = 36–54) display prominent fractionation with extremely high HREE and very low LREE (Figure 7d).

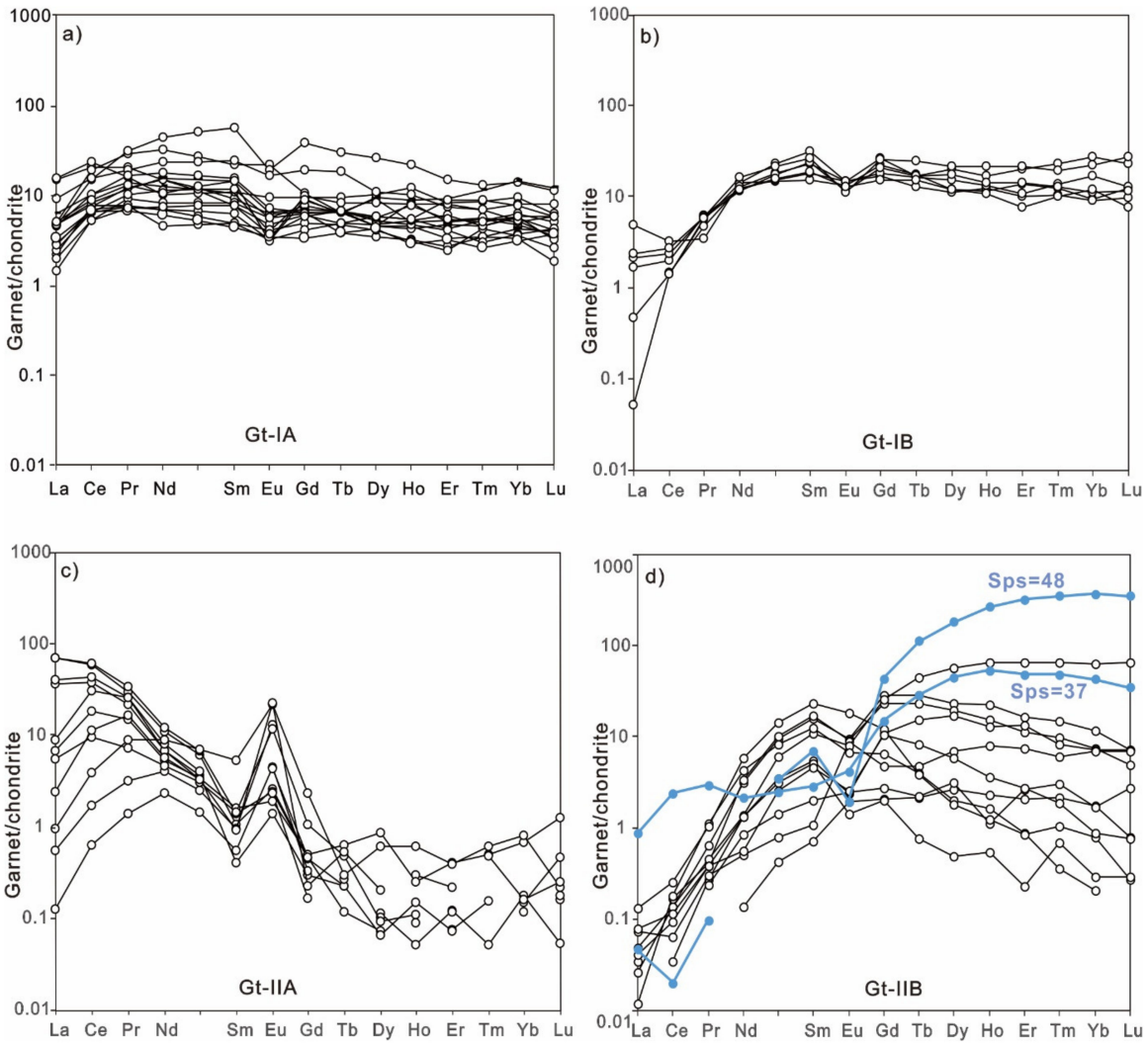

Figure 7. Chondrite-normalized REE patterns of the garnets from the Zhuxiling W (Mo) deposit, chondrite values from [31]. (**a**–**d**) shows REE patterns of Gt-IA, Gt-IB, Gt-IIA and Gt-IIB respectively

and the Mn-rich garnet with high spessartine molecules is marked in blue in Figure 7d. The limit of detection (LOD) is used for the normalized REE patterns when one element value is below the LOD.

LA-ICPMS mapping images of one garnet crystal with a Gt-IA grossular core and Gt-IIA andradite oscillatory rim is presented in Figure 8. The core has relatively homogeneous major and trace element composition, whereas the rim shows rhythmically banded compositional changes corresponding to oscillatory zoning. The mapping results are basically consistent with spot analyses, which shows the Gt-IA garnet of the core is clearly enriched in Al, Ti, and Mg and depleted in Fe and Mn compared with the Gt-II garnet of the rim. The core presents higher contents of Nb and Zr and depleted Sn, In, V, and U compared with the rim. The REE content is characterized by elevated LREE and low HREE for the rim, lacking zoning patterns for HREE.

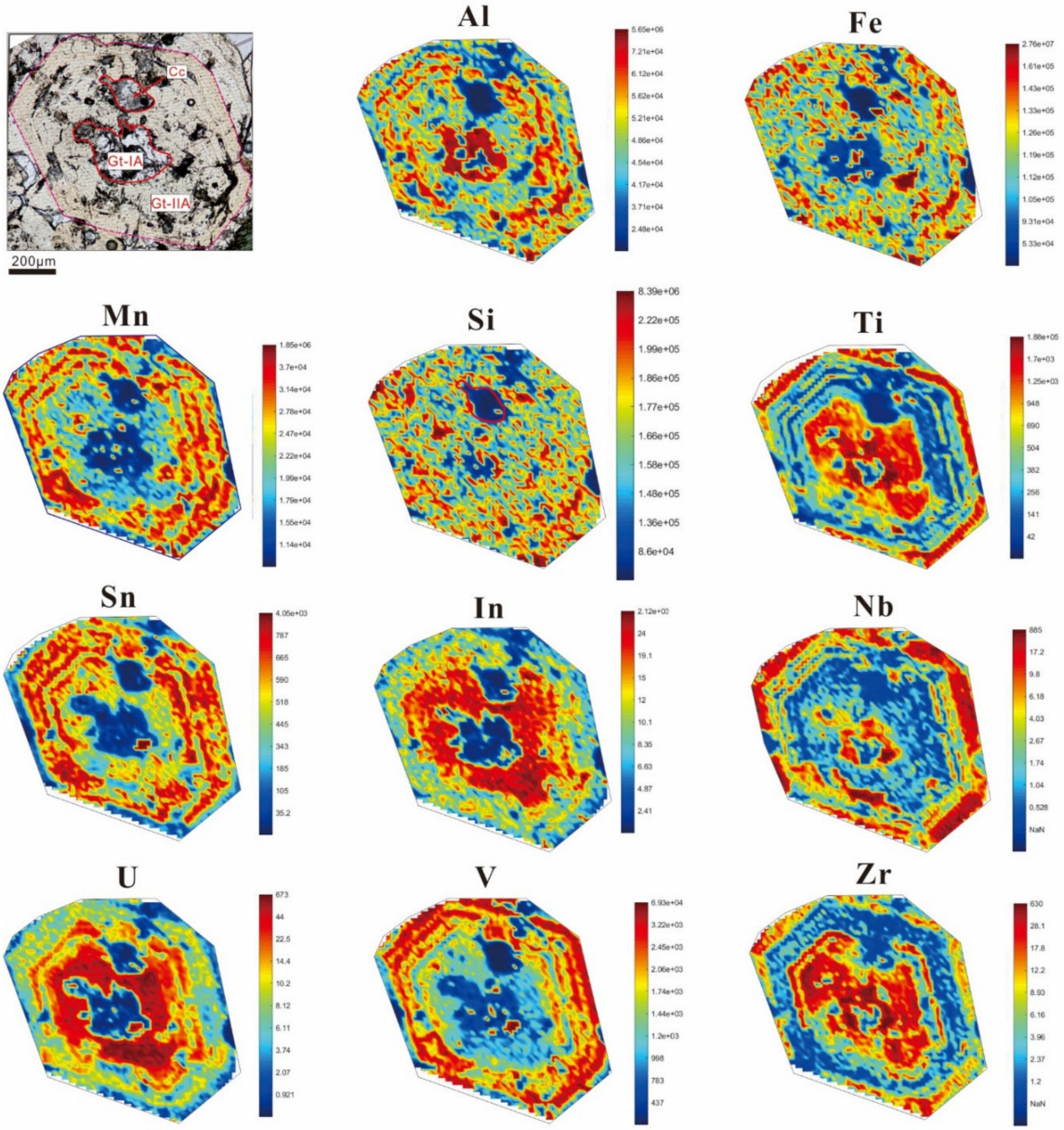

Figure 8. *Cont.*

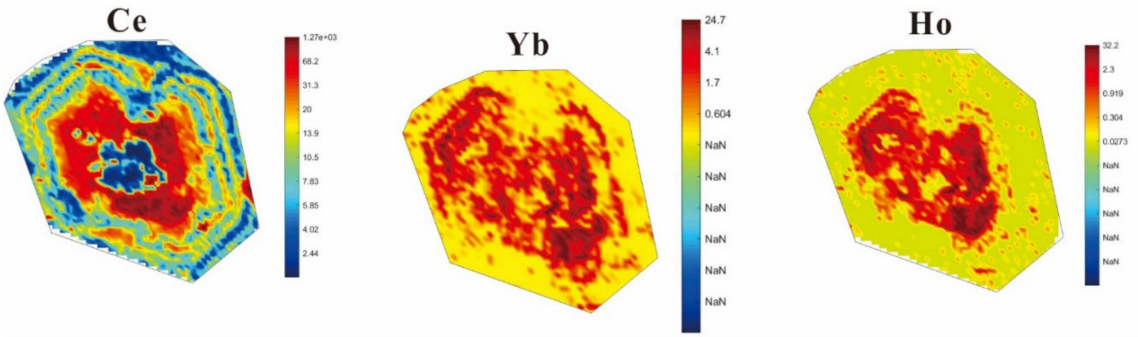

Figure 8. LA-ICPMS probability density maps illustrating element distribution within one garnet crystal with oscillatory-zoned anisotropic rim and isotropic cores, and a calcite inclusion is identified (with very low Si content) and excluded for discussion.

5. Discussion

5.1. Identification of Reduced Skarn System

The tungsten skarn could be divided into reduced and oxidized subtypes based on host rock (carbonaceous versus hematitic), skarn mineralogy (ferrous versus ferric iron ratio), and relative mineralization depth [32]. The reduced W skarn is characterized by lesser grandite garnet in early skarn assemblage and later subcalcic garnet (spessartine and almandine dominant) [1]. The garnets from the Zhuxiling skarn contain significant amount of spessartine and almandine, and the (Sps+Alm) molecule content can reach as high as 56%–68%. The development of subcalcic garnet in Zhuxiling skarn is indicative of a reduced W skarn system. Moreover, associated with subcalcic garnets, the deposit has abundant pyrrhotite and minor sulfides, such as sphalerite and pyrite (Figure 3a). Collectively, the presence of pyrrhotite associated with subcalcic garnet indicate the Zhuxiling skarn belongs to reduced tungsten skarn in comparison to oxidized skarn deposits, such as Kara and King Island deposit [2,3]. Nevertheless, the oxidation state changes during skarn formation indicated by the garnet chemistry. Firstly, the Fe^{2+}/Fe^{3+} ratio is most widely used to reflect oxidation state, which is reflected by the type of garnet and clinopyroxene. For example, Fe-rich andradite with Fe^{3+} as its major composition is considered to be formed under more oxidizing conditions compared with Al-rich grossular [1]. Secondly, the Sn content of garnet could be used as an oxidation indicator. Previous studies have demonstrated that Sn^{4+} substitutes Fe^{3+} at the octathedral site of the garnet lattice [28,33,34], mainly by 1) $Sn^{4+}+Fe^{2+} = 2Fe^{3+}$; 2) $Sn^{4+}+Mg^{2+} = 2Fe^{3+}$; or 3) $3Sn^{4+}+\text{vacancy} = 4Fe^{3+}$. Positive correlation between Sn and andradite molecules of garnets suggests high Sn content is associated with high oxygen fugacity [9]. The Gt-II garnets contain more Fe^{3+} as shown by higher andradite molecules (average Adr = 52) and Sn (average 408 ppm), in contrast to Gt-I garnets (average Adr = 19; Sn = 42 ppm), which implies the former is formed under higher fO_2. Moreover, the Gt-IIA andradite from proximal exoskarn is more Fe-rich and Sn-rich than those of Gt-IIB andradite from distal exoskarn, suggesting a decrease of fO_2 from proximal to distal. The compositional variations of garnet suggested that the oxidization state shifted from a reduced environment of early Gt-I grossular to a relatively oxidized environment of later Gt-II andradite, with the distal exoskarn more reduced than that of proximal skarn.

5.2. Trace Element Incorporation Mechanism

Trace elements could be incorporated into garnet through several ways, such as surface adsorption, occlusion, substitution, and interstitial solid solution [3,35]. Additionally, all those incorporation processes would be influenced by a combination of internal and external factors. The external factors include the fluid composition, P–T condition, fluid/rock ratios, and mineral growth kinetics [4,36,37]. The internal factors mainly refer to crystal-chemical parameters, which play important roles, especially when substitution is the main mechanism. Incorporation mechanisms vary between different elements

for the Zhuxiling garnet. For example, some trace elements of garnets, such as V and Cr, are largely controlled by crystal chemical effects, because V and Cr contents of all garnets show linear correlation with MnO and TiO_2, respectively (Figure 9a,b). However, for REE, U, Zr, and Y, the incorporation mechanism and controlling factors are more complicated.

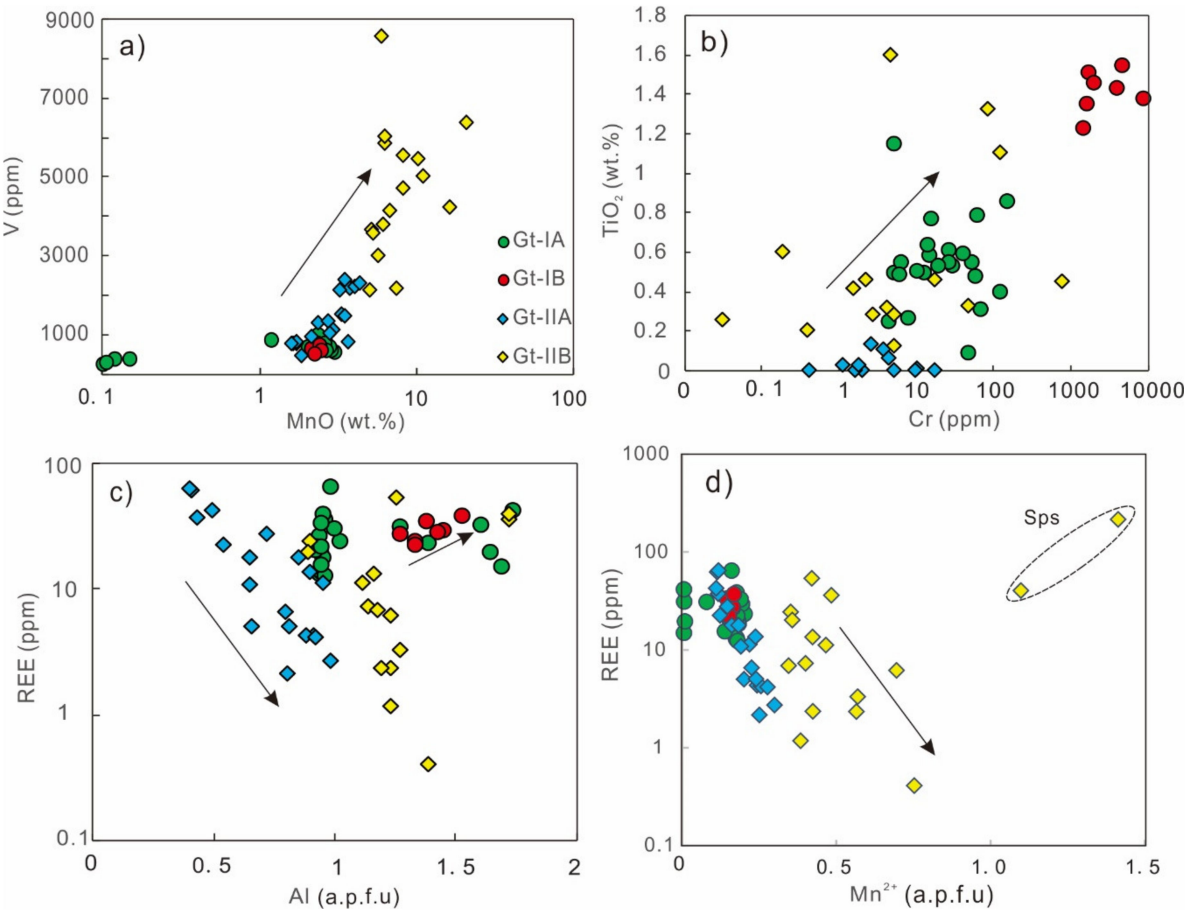

Figure 9. Correlation diagrams of V-Mn, Cr-Ti, Al-REE and Mn-REE of different types of garnets from the Zhuxiling W (Mo) deposit. And (**a**–**d**) represents MnO (%) versus V (ppm), Cr (ppm) versus TiO_2 (%), Al (a.p.f.u) versus REE (ppm), and Mn^{2+} (a.p.f.u) versus REE (ppm) plot respectively.

The incorporation of REE and Y into garnet is basically through the replacement of X^{2+} cations, such as Ca^{2+}, in the dodecahedral position; and the main substitution mechanisms include coupled substitutions, as follows:

$$\left[Ca^{2+}\right]_{-1}^{VIII}\left[REE^{3+}\right]_{+1}^{VIII}\left[Si^{4+}\right]_{-1}^{IV}\left[Al^{3+}\right]_{+1}^{IV},\ \left(REE3^{+} + Al3^{+} = Ca2 + Si4^{+},\ \text{YAG type}\right); \quad (1)$$

$$\left[Ca^{2+}\right]_{-2}^{VIII}\left[Na^{+}\right]_{+1}^{VIII}\left[REE^{3+}\right]_{+1}^{VIII},\ \left(REE3^{+} + Na^{+} = 2Ca2^{+}\right); \quad (2)$$

$$\left[Ca^{2+}\right]_{-3}^{VIII}[\square]_{+1}^{VIII}\left[REE^{3+}\right]_{+2}^{VIII},\ \left(2REE3^{+} + \square = 3Ca2^{+}\right); \quad (3)$$

There is no clear correlation between REE content and Al for Gt-IA grossular garnets, and they contain low Na content, which indicates the incorporation of REE might be controlled by $\left[Ca^{2+}\right]_{-3}^{VIII}[\square]_{-1}^{VIII}\left[REE^{3+}\right]_{+2}^{VIII}$ substitution or the REE incorporation is strongly governed by external factors instead of crystal chemistry control. In contrast, Gt-IB grossular garnets show positive correlation between REE content and Al, which indicates a YAG-type substitution. The REE contents of Gt-II andradite garnets display clear linear relationships with Al, Mn, and Fe^{2+}, which suggest a possible

substitution control. The clearly negative correlation between REE and Al (Figure 9c) disagrees with a YAG-type substitution mechanism. Negative correlation between REE and Fe^{2+} precludes the $\left[Ca^{2+}\right]^{VIII}_{-1}\left[REE^{3+}\right]^{VIII}_{+1}\left[Fe^{2+}\right]^{IV}_{+1}\left[Al^{3+}\right]^{IV}_{-1}$ substitution mechanism suggested by [4]. The presence of an excellent negative correlation with Mn (Figure 9d) leads us to consider REE incorporation of Gt-II garnet might be partially controlled by $\left[Mn^{2+}\right]^{VIII}_{-1}\left[REE^{3+}\right]^{VIII}_{+1}\left[Ca^{2+}\right]^{VIII}_{+1}\left[Al^{3+}\right]^{VIII}_{-1}$ substitution where REE mainly substitute Mn (and Fe^{2+}) in the octathedral site. On the other hand, the wide range of REE and Y content and distinct REE patterns between Gt-IIA and Gt-IIB suggest the incorporation and fractionation of REE is not only controlled by its crystal chemistry, but more importantly by surface adsorption and external factors, such as fluid composition, fluid/rock ratios, and metasomatism dynamics.

5.3. Fluid Evolution and Metasomatic Dynamics

Garnet composition, especially trace elements and REE fractionation, could reflect the external changes and reveal the evolution of fluid chemistry and physical-chemical conditions and trace the fluid–rock interaction and metasomatism dynamics of the skarn system [6,8,30,38,39]. The Gt-I garnet is Al-rich grossular and represents prograde skarn mineral. The concentrated distribution of trace elements and correlation between REE and Y content of Gt-I grossular (Figure 10) indicate Gt-I grossular is formed by diffusive metasomatism under equilibrium conditions. Under such conditions, the growth rate of garnet is constant and low and surface adsorption and diffusivity are negligible according to the kinetics of mineral growth [3]; and variation of trace element composition and fractionation of REE are basically controlled by crystal chemistry and extrinsic P–T–X conditions of fluid. The REE patterns of Gt-IB grossular garnets are typical HREE-enriched and LREE-depleted, consistent with Al-rich garnets reported in other skarn deposits such as Isle of Skye, Ocna de Fier, and Xinqiao skarn. [5,6,8,40]. As mentioned above, REE incorporation of Gt-IB grossular garnet follows a YAG-type substitution, and the corresponding ideal theoretical radius for REE^{3+} is 0.990 Å, with consideration of the radii of Ca^{2+}, Al^{3+}, and Si^{4+} [41]. HREEs are more favorable for substitution than LREEs, since their radii, Tm (0.994 Å), Yb (0.985 Å), and Lu (0.977 Å) in particular, are closer to the ideal theoretical radius. Therefore, the HREE-enriched and LREE-depleted trend of REE for Gt-IB garnet is largely controlled by ionic radius and charges during substitution. On the other hand, Gt-IA grossular garnet exhibits little fractionation between LREE and HREE, and this flat REE pattern may reflect fluid buffered by composition of host rocks due to long residence time of pore fluid under closed-system conditions.

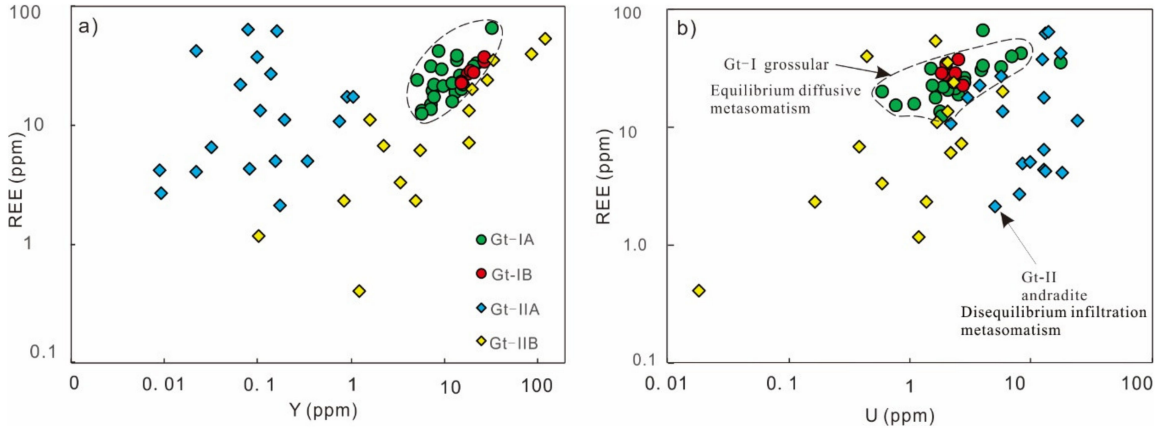

Figure 10. REE and U, Y diagrams of different types of garnets from the Zhuxiling W (Mo) deposit. (**a**) shows Y(ppm) versus REE (ppm) diagram and (**b**) shows U(ppm) versus REE (ppm) diagram.

The Gt-II generation garnet is Fe-rich andradite garnet, which shows common oscillatory zoning. The high Fe^{3+} and Sn content suggests it was formed under oxidized conditions. The development of trapezohedron {211} faces on preexisting dodecahedral {110} garnets (Figure 4D) indicate a fast crystal growth rate under a high fluid/rock ratio [42,43]. Additionally, Gt-II garnet displays dramatic compositional variation, as shown by patched BSE imaging within a single sample (Figure 4F) and scattered REE, Y, and U concentrations (Figure 10), which reflect infiltration metasomatism under disequilibrium conditions in an open system. Fluid fluctuation variations in the open system would facilitate the formation of oscillatory zoning. The trace elements and REE of Gt-II andradite garnet are predominantly controlled by external factors combined with partially crystal chemistry impact. The enriched-LREE and significantly positive Eu anomaly of Gt-IIA garnet are attributed to the following factors: (1) The calculation of enthalpy of mixing between REEAl and REEFe garnet components suggested the HREE are more soluble than the LREE in both grossular and andradite, whereas static interactions taking place in grandite mixtures can lead to opposite trends. High andradite-rich mixtures host more LREE relative to HREE due to a static interaction effect [3]. The Gt-IIA andradite garnets have high andradite molecules (37–85) and the LREE-enriched and HREE-depleted trend of REE, consistent with this crystal chemistry effect. (2) Since Gt-IIA andradite garnet is formed under high fluid/rock ratios in an open system and its REE pattern mimics the hydrothermal fluid composition due to the partition coefficient of unity between garnet and fluid [3]. The REE signature of andradite reflects characteristics of magmatic fluid, which is reported to have enriched LREE and depleted HREE with a variable Eu anomaly [44–46]. (3) As mentioned above, the skarn of the Zhuxiling W (Mo) deposit was formed under a reduced environment and Eu mainly occur in the form of Eu^{2+} in grandite garnet under such conditions. Recent studies verify Cl^- and SO_4^{2-} complexes are major agents for transporting REE^{3+} in hydrothermal fluid [47–49] and chloride complex dominant under low PH conditions [38]. There is no chemical or mineralogical evidence for SO_4^{2-}, and thus chlorine might play a major role. Moreover, chlorine enhances the stability of soluble Eu^{2+} ($EuCl_4^{2-}$ the dominant species) in reduced and slightly acidic fluids at high temperatures (400 °C, [39]), which would lead to positive Eu anomalies. Besides, the Cl-rich fluid bonds with LREE more strongly compared with HREE [50], which fits with LREE-enriched pattern of Gt-IIA andradite garnet.

The Gt-IIB andradite garnet displays a reversed REE pattern with enriched HREE and depleted LREE. The following reasons are considered responsible for the change in REE fractionation from proximal to distal skarn: (1) Continuous crystallization of Fe-rich andradite in proximal exoskarn (Adr 37-85 and enriched in LREE) consumes large amounts of Fe as well as LREE of the fluid and leads to the depletion of Fe and LREE of a subsequent fluid, which formed the distal exoskarn. (2) Lower andradite end-member contents (Adr 8-60 for Gt-IIB) favor the HREE incorporation relative to LREE based on the calculation of enthalpy of mixing between the REEAl and REEFe garnet components, and HREE is preferred during garnet–fluid partitioning [3,51]. This crystal chemistry effect further enhanced LREE depletion and HREE enrichment.

5.4. Formation of Garnets in the Dynamic Skarn System

The first generation garnet is Al-rich grossular formed by diffusive metasomatism with equilibrium with fluids under relatively reduced environment. The elevated contents of Ti and Mn combined with the euhedral to subhedral form and scarce occurrence reveal that Gt-IB grossular garnet represents endoskarn mineral formed very early in prograde-stage, with more incorporation of Ti, Mn, V, and Cr from the intrusion. In contrast, Gt-IA grossular garnet is anhedral and is replaced by latter Gt-II garnet. It represents prograde skarn mineral formed from fluid buffered by composition of host rocks by diffusive metasomatism. The variation of trace element composition and fractionation of REE of the first generation garnet are basically controlled by crystal chemistry and extrinsic P–T–X conditions of fluid. The diffusive metasomatism is responsible for the concentrated REE and Y contents of Gt-I grossular garnet. REE fractionation of Gt-IA garnet is impacted by fluid–water interaction

in equilibrium with pore water. In addition, the REE pattern of Gt-IB garnet is largely controlled by crystal chemistry through substitution.

The second generation garnet is Fe-rich andradite, which represents rapid growth garnet formed by infiltration metasomatism with a high water/rock ratio in an open system. Gt-IIA andradite garnets from proximal exoskarn are Fe-rich and LREE-enriched andradite and continuous crystallization of proximal exoskarn consumes large amounts of Fe and consequently leads to the depletion of andradite in the distal exoskarn. Furthermore, garnet shows compositional changes with a decrease of Fe and an increase of Mn, from proximal skarn (Gt-IIA garnet) to distal skarn (Gt-IIB garnet) with enormously high spessartine molecules of 36%–54% for some Gt-IIB garnets. A previous study suggests that Mn-rich garnet forms early crystallization on the contact zone with marble [52]. In this study, the Mn-rich dolomitic limestone of the Lantian Group [24] is most likely the major Mn source for spessartine in Gt-IIB garnets. The presence of Mn-rich garnet implies the fluid must have actively interacted with Mn-rich dolomitic limestone in the distal skarn formation. The trace element and REE signatures of Gt-II andradite garnet are predominantly controlled by external factors and partly by crystallographic properties. The REE patterns of Gt-IIA garnet mainly reflects the characteristics of magmatic fluid, and the positive Eu anomaly suggests chlorine might play a major role as a complex agent ($EuCl_4^{2-}$ the dominant species), which also bonds more strongly with LREE compared with HREE [46,50]. On the contrary, Gt-IIB garnet shows reversed REE patterns compared with Gt-IIA garnet. The change in REE characteristics is possibly caused by the massive consumption of LREE by the crystallization of Fe-rich andradite garnets in the proximal skarn and assisted by a crystal chemical effect. Garnet compositional variations of the two generations and four different types suggest the skarn system evolved from reduced closed conditions gradually to more oxidized, open conditions with fracturing.

6. Conclusions

1) Two generations of garnet have been identified for the Zhuxiling W (Mo) skarn: Gt-I generation garnet is Al-rich grossular ($Adr_{3\text{-}46}Grs_{49\text{-}96}$ $(Sps+Pyr+Alm)_{1\text{-}5}$) and Gt-II generation garnet is Fe-rich andradite. The proximal exoskarn Gt-IIA type garnet is more Fe-rich andradite ($Adr_{37\text{-}85}Grs_{4\text{-}58}(Sps+Pyr+Alm)_{4\text{-}19}$) than Gt-IIB andradite ($Adr_{8\text{-}60}Grs_{18\text{-}47}$ $(Sps+Pyr+Alm)_{11\text{-}68}$), whereas Gt-IIB garnet is Mn-rich, with spessartine and almandine molecule contents as high as 56%–68%. The presence of pyrrhotite associated with subcalcic garnet indicates a relatively reduced tungsten skarn system.
2) Both W and Sn strongly favor Fe-rich garnet compared with Al-rich garnet. Gt-IA grossular garnet presents a flat REE trend and Gt-IB grossular has a distinct REE pattern with enriched HREE. Gt-IIA andradite garnet displays a right-dipping REE trend with a prominent positive Eu anomaly. In comparison, Gt-IIB andradite garnet features depleted LREE and enriched HREE with weak positive Eu anomaly. The REE fractionation of Gt-IB grossular garnet is predominantly controlled by YAG-type substitution, whereas Gt-IA and Gt-II garnets are collectively controlled by crystal chemistry and the external P–T–X condition of fluids.
3) The first generation Al-rich grossular garnets grow slowly under a closed system, whereas the latter formed Fe-rich andradite garnets represent rapid growth garnet associated with magmatic fluids in an open system. Garnet shows compositional changes with a decrease of Fe and an increase of Mn from proximal skarn (Gt-IIA garnet) to distal skarn (Gt-IIB garnet) due to more active fluid–rock interaction with Mn-rich dolomitic limestone of the Lantian Group in the district.

Supplementary Materials: The following are available online at http://www.mdpi.com/2075-163X/10/11/1024/s1. Table S1: EPMA major elements data of garnets from the Zhuxiling W (Mo) deposit; Table S2: LA-ICPMS trace element data of garnets from the Zhuxiling W (Mo) deposit.

Author Contributions: Field work, X.-X.D., Z.-Q.W., and B.C.; experiment, X.-X.D. and Y.-F.J.; data analysis, X.-X.D. and Y.-F.J.; original draft preparation, X.-X.D., Y.-F.J. and B.C.; revision and editing, X.-X.D. and Z.-Q.W. All authors have read and agreed to the published version of the manuscript.

Funding: This research was funded by the National Key Research and Development Project [No. 2016YFC0600108-03-2] and National Nature Science Foundation of China [No.41530206].

Acknowledgments: We thank Dr. Wang Juan and Wang Fangyue of HFUT for their assistance during the EPMA and LA-ICPMS analysis. We would like to express our gratitude to Sun Keke and Professor Wang De'en for their support in the field work. Appreciation is given to Professor Thomas Ulrich and three anonymous reviewers for their careful review and advice. We thank Dr. Zhou Lingli for the organization of this special issue.

Conflicts of Interest: The authors declare no conflict of interest.

References

1. Meinert, L.D.; Dipple, G.M.; Nicolescu, S. World skarn deposits. In *Economic Geology 100th Anniversary Volume*; Hedenquist, J.W., Thompson, J.F.H., Goldfarb, R.J., Richards, J.P., Eds.; Society of Economic Geologists: Littleton, CO, USA, 2005; pp. 299–336.
2. Zaw, K.; Singoyi, B. Formation of magnetite-scheelite skarn mineralization at Kara, Northwestern Tasmania: Evidence from mineral chemistry and stable isotopes. *Econ. Geol.* **2000**, *95*, 1215–1230. [CrossRef]
3. Gaspar, M.; Knaack, C.; Meinert, L.D.; Moretti, R. REE in skarn systems: A LA–ICP–MS study of garnets from the crown jewel gold deposit. *Geochim. Cosmochim. Acta* **2008**, *72*, 185–205. [CrossRef]
4. Ding, T.; Ma, D.S.; Lu, J.J.; Zhang, R.Q. Garnet and scheelite as indicators of multi-stage tungsten mineralization in the Huangshaping deposit, southern Hunan province, China. *Ore Geol. Rev.* **2018**, *94*, 193–211. [CrossRef]
5. Xiao, X.; Zhou, T.F.; Noel, C.W.; Zhang, L.J.; Fan, Y.; Wang, F.Y.; Chen, X.F. The formation and trace elements of garnet in the skarn zone from the Xinqiao Cu-S-Fe-Au deposit, Tongling ore district, Anhui Province, Eastern China. *Lithos* **2018**, *302–303*, 467–479. [CrossRef]
6. Smith, M.P.; Henderson, P.; Jeffries, T.E.R.; Long, J.; Williams, C.T. The rare earth elements and uranium in garnets from the Beinnan Dubhaich Aureole, Skye, Scotland, UK: Constraints on processes in a dynamic hydrothermal system. *J. Petrol.* **2004**, *45*, 457–484. [CrossRef]
7. Somarin, A.K. Garnet composition as an indicator of Cu mineralization: Evidence from skarn deposits of NW Iran. *J. Geochem. Explor.* **2004**, *81*, 47–57. [CrossRef]
8. Park, C.P.; Song, Y.G.; Kang, I.M.; Shim, J.; Chung, D.H.; Park, C.S. Metasomatic changes during periodic fluid flux recorded in grandite garnet from the Weondong Wskarn deposit, South Korea. *Chem. Geol.* **2017**, *451*, 135–153. [CrossRef]
9. Zhou, J.H.; Feng, C.Y.; Li, D.X. Geochemistry of the garnets in the Baiganhu W-Sn orefield, NW China. *Ore Geol. Rev.* **2017**, *82*, 70–92. [CrossRef]
10. Yang, Y.L.; Ni, P.; Wang, Q.; Wang, J.Y.; Zhang, X.L. In situ LA-ICP-MS study of garnets in the Makeng Fe skarn deposit, eastern China: Fluctuating fluid flow, ore-forming conditions and implication for mineral exploration. *Ore Geol. Rev.* **2020**, *126*, 103725. [CrossRef]
11. Mao, J.W.; Xiong, B.K.; Liu, J.; Pirajno, F.; Cheng, Y.B.; Ye, H.S.; Song, S.W.; Dai, P. Molybdenite Re/Os dating, zircon U-Pb age and geochemistry of granitoids in the Yangchuling porphyry W-Mo deposit Jiangnan tungsten ore belt, China: Implications for petrogenesis, mineralization and geodynamic setting. *Lithos* **2017**, *296–297*, 35–52. [CrossRef]
12. Song, G.X.; Qin, K.Z.; Li, G.M.; Eavans, N.J.; Chen, L. Scheelite elemental and isotopic signatures: Implications for the genesis of skarn-type W(Mo) deposits in the Chizhou Area, Anhui Province, Eastern China. *Am. Mineral.* **2014**, *99*, 303–317. [CrossRef]
13. Song, G.X.; Qin, K.Z.; Li, G.M.; Li, X.; Qu, W. Geochronology and ore-forming fluids of the Baizhangyan W-Mo Deposit in the Chizhou Area, Middle-Lower Yangtze Valley, SE China. *Res. Geol.* **2013**, *63*, 57–71. [CrossRef]
14. Zhang, D.Y.; Zhou, T.F.; Yuan, F.; Fan, Y.; Chen, X.F.; White, N.C.; Ding, N.; Jiang, Q.S. Petrogenesis and W(Mo) fertility indicators of the Gaojiabang "satellite" granodiorite porphyry in southern Anhui Province, South China. *Ore Geol. Rev.* **2017**, *88*, 550–564. [CrossRef]
15. Su, Q.W.; Mao, J.W.; Wu, S.H.; Zhang, Z.C.; Xu, S.F. Geochronology and geochemistry of the granitoids and ore-forming age in the Xiaoyao tungsten polymetallic skarn deposit in the Jiangnan Massif tungsten belt, China: Implications for their petrogenesis, geodynamic setting, and mineralization. *Lithos* **2018**, *296–299*, 365–381. [CrossRef]

16. Wang, X.L.; Zhou, J.C.; Griffin, W.L.; Wang, R.C.; Qiu, J.S.; O'Reilly, S.Y.; Xu, X.S.; Liu, X.M.; Zhang, G.L. Detrital zircon geochronology of Precambrian basement sequences in the Jiangnan orogen: Dating the assembly of the Yangtze Cathaysia blocks. *Precambrian Res.* **2007**, *159*, 117–131. [CrossRef]
17. Zhang, C.L.; Santosh, M.; Zou, H.B.; Li, H.K.; Huang, W.C. The Fuchuan ophiolite in Jiangnan Orogen: Geochemistry, zircon U-Pb geochronology, Hf isotope and implications for the Neoproterozoic assembly of South China. *Lithos* **2013**, *179*, 263–274. [CrossRef]
18. Yao, J.; Shu, L.; Santosh, M.; Li, J. Neoproterozoic arc–related andesite and orogeny–related unconformity in the eastern Jiangnan orogenic belt: Constraints on the assembly of the Yangtze and Cathaysia blocks in South China. *Precambrian Res.* **2015**, *262*, 80–100. [CrossRef]
19. Mao, Z.H.; Liu, J.J.; Mao, J.W.; Deng, J.; Zhang, F.; Meng, X.Y.; Xiong, B.K.; Xiang, X.K.; Luo, X.H. Geochronology and geochemistry of granitoids related to the giant Dahutang tungsten deposit, middle Yangtze River region, China: Implications for petrogenesis, geodynamic setting, and mineralization. *Gondwana Res.* **2015**, *29*, 816–836. [CrossRef]
20. Geological Survey of Anhui Province (GSAP). *Geological Report of the Anhui Tungsten (Tin and Molybdenum) Mineral Resources Potential Evaluation*; Geological Survey of Anhui Province (GSAP): Anhui, China, 2011; p. 263.
21. Ding, N. Metallogenic Regularity of Tungsten Deposits in Anhui Province. Master's Thesis, Hefei University of Technology, Hefei, China, 2012; p. 154. (In Chinese).
22. Yan, J.; Hou, T.J.; Wang, A.G.; Wang, D.E.; Zhang, D.Y.; Weng, W.F.; Liu, J.M.; Liu, X.Q.; Li, Q.Z. Petrogenetic contrastive studies on the Mesozoic early stage ore-bearing and late stage ore-barren granites from the southern Anhui Province. *Sci. China Earth Sci.* **2017**, *60*, 1920–1941. [CrossRef]
23. Zhou, T.F.; Wang, S.W.; Fan, Y.; Yuan, F.; Zhang, D.Y.; White, N.C. A review of the intracontinental porphyry deposits in the Middle-Lower Yangtze River Valley metallogenic belt, Eastern China. *Ore Geol. Rev.* **2015**, *65*, 433–456. [CrossRef]
24. Huang, M. Metallogenetic Ages and Geochemical Characteristics of Zhuxiling W-Ag Polymetallic Deposit in Ningguo City, Southern Anhui Province. Master's Thesis, Hefei University of Technology, Hefei, China, 2017; p. 64. (In Chinese).
25. Chen, X.F.; Wang, Y.G.; Sun, W.D.; Yang, X.Y. Zircon U-Pb chronology, geochemistry and genesis of the Zhuxiling granite in Ningguo, Southern Anhui. *Acta Geol. Sin.* **2013**, *87*, 1662–1678. (In Chinese)
26. Wang, Y.; van den Kerkhof, A.; Xiao, Y.; Sun, H.; Yang, X.; Lai, J.; Wang, Y. Geochemistry and fluid inclusions of scheelite-mineralized granodiorite porphyries from southern Anhui Province, China. *Ore Geol. Rev.* **2017**, *89*, 988–1005. [CrossRef]
27. Duan, X.X.; Chen, B.; Sun, K.K.; Wang, Z.Q.; Yan, X.; Zhang, Z. Accessory mineral chemistry as a monitor of petrogenetic and metallogenetic processes: A comparative study of zircon and apatite from Wushan Cu- and Zhuxiling W(Mo)-mineralization-related granitoids. *Ore Geol. Rev.* **2019**, *111*, 102940. [CrossRef]
28. Chen, J.; Halls, C.; Stanley, C.J. Tin-bearing skarns of South China: Geological setting and mineralogy. *Ore Geol. Rev.* **1992**, *7*, 225–248. [CrossRef]
29. Yao, Y.; Chen, J.; Lu, J.J.; Zhang, R.Q.; Zhao, L.H. Composition, trace element and infrared spectrum of garnet from three types of W-Sn bearing skarns in the South of China. *Acta Mineral. Sin.* **2013**, *33*, 315–329. (In Chinese)
30. Van Westrenen, W.; Allan, N.L.; Blundy, J.D.; Purton, J.A.; Wood, B.J. Atomistic simulation of trace element incorporation into garnets-comparison with experimental garnet-melt partitioning data. *Geochim. Cosmochim. Acta* **2000**, *64*, 1629–1639. [CrossRef]
31. Sun, S.S.; McDonough, W.F. Chemical and isotopic systematics of oceanic basalts: Implications for mantle composition and processes. *Geol. Soc. Spec. Publ.* **1989**, *42*, 313–345. [CrossRef]
32. Newberry, R.J.; Einaudi, M. T Tectonic and geochemical setting of tungsten skarn mineralization in the Cordillera. *Ariz. Geol. Soc. Dig.* **1981**, *14*, 99–111.
33. Butler, B.C.M. Tin-rich garnet, pyroxene, and spinel from a slag. *Mineral. Mag.* **1978**, *42*, 487–492. [CrossRef]
34. Amthauer, G.; McIver, J.R.; Viljoen, E.A. ^{57}Fe and ^{119}Sn Mössbauer studies of natural tin-bearing garnets. *Phys. Chem. Miner.* **1979**, *4*, 235–244. [CrossRef]
35. McIntire, W.L. Trace element partition coefficients—A review of theory and applications to geology. *Geochim. Cosmochim. Acta* **1963**, *27*, 1209–1264. [CrossRef]
36. Jamtveit, B.; Hervig, R.L. Constraints on transport and kinetics in hydrothermal systems from zoned garnet crystals. *Science* **1994**, *263*, 505–508. [CrossRef] [PubMed]

37. Chernoff, C.B.; Carlson, W.D. Trace element zoning as a record of chemical disequilibrium during garnet growth. *Geology* **1999**, *27*, 555–558. [CrossRef]
38. Bau, M. Rare-earth element mobility during hydrothermal and metamorphic fluid-rock interaction and the significance of the oxidation state of europium. *Chem. Geol.* **1991**, *93*, 219–230. [CrossRef]
39. Allen, D.E.; Seyfried, W.E. REE controls in ultramafic hosted MOR hydrothermal systems: An experimental study at elevated temperature and pressure. *Geochim. Cosmochim. Acta* **2005**, *69*, 675–683. [CrossRef]
40. Nicolescu, S.; Cornell, D.H.; Sodervall, U.; Odelius, H. Secondary ion mass spectrometry analysis of rare earth elements in grandite garnet and other skarn related silicates. *Eur. J. Mineral.* **1998**, *10*, 251–259. [CrossRef]
41. Shannon, R.D. Revised effective ionic radii and systematic studies of interatomic distances in halides and calcogenides. *Acta Crystallogr.* **1976**, *32*, 751–767. [CrossRef]
42. Jamtveit, B.; Wogelius, R.A.; Fraser, D.G. Zonation patterns of skarn garnets: Records of hydrothermal system evolution. *Geology* **1993**, *21*, 113–116. [CrossRef]
43. Jamtveit, B. Oscillatory zonation patterns in hydrothermal grossular-andradite garnet. Nonlinear dynamics in regions of immiscibility. *Am. Mineral.* **1991**, *76*, 1319–1327.
44. Kravchuk, I.F.; Ivanova, G.F.; Varezhkina, N.S.; Malinin, S.D. REE fractionation in acid fluid-magma systems. *Geochem. Intern.* **1995**, *32*, 60–68.
45. Reed, M.J.; Candela, P.A.; Piccoli, P.M. The distribution of rare earth elements between monzogranitic melt and the aqueous volatile phase in experimental investigations at 800 C and 200 MPa. *Contrib. Mineral. Petrol.* **2000**, *140*, 251–262. [CrossRef]
46. Yang, X.M. Using Rare Earth Elements (REE) to decipher the origin of ore fluids associated with granite intrusions. *Minerals* **2019**, *9*, 426. [CrossRef]
47. Mayanovic, R.A.; Anderson, A.J.; Bassett, W.A.; Chou, I.M. On the formation and structure of rare-earth element complexes in aqueous solutions under hydrothermal conditions with new data on gadolinium aquo and chloro complexes. *Chem. Geol.* **2007**, *239*, 266–293. [CrossRef]
48. Migdisov, A.A.; Williams-Jones, A.E. Hydrothermal transport and deposition of the rare earth elements by fluorine-bearing aqueous liquids. *Miner. Depos.* **2014**, *49*, 987–997. [CrossRef]
49. Xing, Y.; Etschmann, B.; Liu, W.; Mei, Y.; Testemale, D.; Shvarov, Y.; Tomkins, A.; Brugger, J. The role of fluorine in hydrothermal mobilization and transportation of Fe, U and REE and the formation of IOCG deposits. *Chem. Geol.* **2019**, *504*, 158–176. [CrossRef]
50. Rolland, Y.; Cox, S.; Boullier, A.-M.; Pennacchioni, G.; Mancktelow, N. Rare earth and trace element mobility in mid-crustal shear zones: Insights from the Mont Blanc Massif (Western Alps). *Earth Planet Sci. Lett.* **2003**, *214*, 203–219. [CrossRef]
51. Moretti, R.; Ottonello, G. An appraisal of endmember energy and mixing properties of the rare earth garnets. *Geochim. Cosmochim. Acta* **1998**, *62*, 1147–1173. [CrossRef]
52. Einaudi, M.T.; Meinert, L.D.; Newberry, R.J. Skarn deposits. *Econ. Geol.* **1981**, *75*, 317–391.